

# Effects of Geometric configuration in Relativistic isobaric collisions at $\sqrt{s_{NN}} = 200$ GeV

Akash Das<sup>1,\*</sup>, Satya Ranjan Nayak<sup>2,†</sup> and B. K. Singh<sup>1,2‡</sup>

<sup>1</sup>*Discipline of Natural Sciences,  
PDPM Indian Institute of Information Technology Design & Manufacturing,  
Jabalpur 482005, INDIA.*

<sup>2</sup>*Department of Physics, Institute of Science,  
Banaras Hindu University (BHU),  
Varanasi, 221005, INDIA.*

(Dated: August 26, 2025)

In this work, we present a study on the effects of nuclear deformation ( $\beta_2, \beta_3$ ) and surface diffuseness ( $a$ ) on the charged hadron multiplicity ( $N_{ch}$ ) and elliptic flow ( $v_2$ ), obtained in symmetric isobaric collisions of  $^{96}_{44}\text{Ru} + ^{96}_{44}\text{Ru}$  and  $^{96}_{40}\text{Zr} + ^{96}_{40}\text{Zr}$ . The two extreme configurations (tip-tip and body-body) were used to determine the correlation between the final state observables and initial geometry using the HYDJET++ model. The octupole deformation parameter ( $\beta_3$ ) enhances  $N_{ch}$  in central tip-tip Zr+Zr collisions and suppresses it in peripheral ones. In mid-central to peripheral body-body Zr+Zr collisions,  $\beta_3$  leads to a reduction in charged hadron production. Surface-diffuseness ( $a$ ), along with quadrupole deformation ( $\beta_2$ ), also shows a significant impact on multiplicity and elliptic flow. The octupole deformation enhances elliptic flow in Zr's body-body collisions. Results are compared with the STAR blind-analysis data where available.

## I. INTRODUCTION

Charge-Parity (CP) violation is a phenomenon through which we can understand the existence of our matter-dominated universe [1]. There is evidence of CP violation in weak decay [2, 3], but it is still not experimentally proven in strong interactions. Recent experiments in the Relativistic Heavy-Ion Collider (RHIC) and the Large Hadron Collider (LHC) give positive hints of possible CP-violating effects in Quark-Gluon Plasma (QGP) [4, 5]. Relativistic heavy-ion collisions in collider experiments may produce such extreme conditions, where the strong interaction locally violates parity (P) and charge parity (CP) symmetries [6–9]. This violation would result in an imbalance between the right-handed and left-handed quarks in the QGP. In an off-center heavy-ion collision, the spectator protons in the colliding nuclei create a strong magnetic field (B) [10], which may interact with the chiral imbalance and segregate charges along the field direction. This charge separation phenomenon is called the chiral magnetic effect (CME) [11–15].

Initially, the idea of isobar collision was proposed to overcome the large background noise (especially flow-induced background), which makes it difficult to observe CME. The key idea was that, since isobars have the same mass number, this can lead to a similar background. But due to different proton numbers, it should result in different strengths of magnetic field and hence different CME signals [16].

Taking this into consideration, collisions of the isobars  $^{96}_{44}\text{Ru} + ^{96}_{44}\text{Ru}$  and  $^{96}_{40}\text{Zr} + ^{96}_{40}\text{Zr}$  are conducted at the RHIC

STAR experiment, primarily focused on obtaining signals regarding the CME. It was highly anticipated that visible evidence of CME might be found. But the STAR collaboration's blind analysis data of isobar collision didn't find evidence of the CME based on their predefined criteria [17]. Rather, they discovered that the two collision systems had different CME backgrounds due to differences in the number of charged hadron generation ( $N_{ch}$ ) and collective flow harmonics ( $v_n$ ) [18]. The two nuclei's differing geometrical shapes can be directly linked to the observed discrepancy in the CME background [19].

In the Woods-Saxon (WS) distribution, the diffuseness parameter ( $a$ ) characterizes the surface thickness of the nucleus — that is, how smoothly the nuclear density transitions from its central value to zero at the edge. Ru exhibits a larger quadrupole deformation ( $\beta_2$ ), whereas Zr shows a stronger octupole deformation ( $\beta_3$ ) [20]. Because of the smaller multiplicity in Ru+Ru and Zr+Zr collisions, the background signal in these systems is approximately twice that in Au+Au collisions. In contrast, the CME signal is expected to be about half of that in Au+Au collisions, owing to the weaker magnetic field [16]. Therefore, it is crucial to understand the contributions of background signals in Ru and Zr, as well as the influence of deformation on these signals. The investigation of small-scale CME signals can proceed once the backgrounds have been thoroughly understood.

During the fireball's evolution immediately following a collision, the initial spatial anisotropy transfers into the final momentum anisotropy [21]. If the deformation parameters of Ru and Zr are incorporated into the simulation, they affect the initial-state geometry and consequently, the final flow observables [22].

The anisotropy in the momentum is usually quantified using the Fourier expansion of particle density with respect to the azimuthal angle  $\phi$  [23],

\* 24pnp01@iiitdmj.ac.in

† satyanayak@bhu.ac.in

‡ bksingh@bhu.ac.in; director@iiitdmj.ac.in

$$\frac{dN}{d\phi} \propto 1 + 2 \sum_{n=1}^{\infty} v_n \cos[n(\phi - \psi_n)] \quad (1)$$

where  $\phi$  is the azimuthal angle of the produced particle,  $v_n$  is the  $n$ 'th order Fourier coefficient and  $\psi_n$  is the angle of the reaction plane.

We begin our analysis with a spherical nuclear configuration (i.e., no deformation), and subsequently incorporate deformation effects by considering two extreme geometrical configurations: tip-tip and body-body collisions. The objective is to investigate the effects of these specific geometrical configurations by analyzing the charged hadron pseudorapidity density ( $\frac{dN_{ch}}{d\eta}$ ), the number of charged hadrons ( $N_{ch}$ ) and the elliptic flow coefficients ( $v_2$ ).

This article is organized as follows:- In section II, we have discussed broadly about the HYDJET++ model. In section III, we provide the results and discussions part under three sections: (A) Pseudorapidity distribution, (B)  $N_{ch}$  distribution analysis, and (C)  $v_2$  ratio. In section IV, a comprehensive summary of our work is presented.

## II. HYDJET++

The HYDJET++ is a Monte Carlo event generator, commonly used for the simulation of relativistic heavy-ion collisions. The HYDJET++ model superposes both the soft hydro-type state and the hard state independently, yet simultaneously. The model uses Bjorken's solution of ideal hydrodynamics [24] for space-time evolution of the fireball, hence the model calculations better describe mid-rapidity data. At forward rapidities, one should use Landau hydrodynamics [25] for a more accurate description of medium expansion. A detailed physics framework of the model and simulation can be seen in these articles [26, 27]. The key points are outlined below:-

**Hard Part:-** HYDJET++ models the hard interactions using the PYTHIA Quenched (PYQUEN) partonic energy loss model [28]. The initial particle spectra are generated by PYTHIA 6 [29]. Later, PYQUEN modifies the initial particle spectra by generating binary nucleon-nucleon collision vertices at a specified impact parameter, following the Glauber Model [30]. In PYTHIA, the parameter  $p_T^{\min}$  separates the hard part from the soft part. If the momentum transfer in individual interactions is greater than  $p_T^{\min}$ , i.e.,  $p_T > p_T^{\min}$ , then these interactions are considered as hard processes by PYQUEN. Moreover for the interactions  $p_T < p_T^{\min}$ , they are considered as soft process. PYQUEN does an event-by-event calculation on re-scattering of partons via integrating the radiation and collisional energy losses [24, 31] inside the medium. Finally, hadronization is done according to the Lund string fragmentation model [32].

**Soft Part:-** The soft part of HYDJET++ is a thermal hadronic state, which is generated on the chemical and thermal freeze-out hypersurfaces obtained from a parametrization of relativistic hydrodynamics with preset freeze-out conditions [33, 34]. The QGP created in collision reaches a local equilibrium just after a short period of time ( $< 1 fm/c$ ) and further expands hydrodynamically. In HYDJET++, chemical and thermal freeze-outs are assumed to happen separately because at chemical freezeout, the density of the particles is too high to consider them as free streaming. So, a more complex but relevant condition of  $T_{ch} \leq T_{th}$  is used. The system expands hydrodynamically with frozen chemical composition in between the two freezeout conditions, then it cools down, and hadrons start moving freely after they reach the thermal freezeout temperature.

**Elliptic Flow:-** Shortly after the collision (preferably peripheral), an asymmetric almond shape is formed in the overlap region. It produces a pressure gradient, generally stronger towards the shorter axis of the ellipse. This initial anisotropy transfers into momentum anisotropy, and the flow phenomenon is called elliptic flow [35]. And  $v_2$  can be defined in terms of particle momenta-

$$v_2 = \left\langle \frac{p_x^2 - p_y^2}{p_x^2 + p_y^2} \right\rangle = \left\langle \frac{p_x^2 - p_y^2}{p_T^2} \right\rangle \quad (2)$$

Rather than using the microscopic transport model AMPT [36], or the Hydrodynamic model MUSIC [37], which have a proper evolution stage but are computationally tedious, HYDJET++ follows a simpler idea of parametrization of freeze-out hypersurface for getting elliptic flow. For that purpose, in HYDJET++, we have two coefficients:- spatial anisotropy  $\epsilon_2$  and momentum anisotropy  $\delta_2$ , respectively. Generally, these two are taken as free parameters, but in our work, we have taken them as a function of impact parameter, so that the radius of the fireball changes with collision geometry. Spatial anisotropy  $\epsilon_2$  demonstrates the elliptic modulation of the final freeze-out hypersurface, and  $\delta_2$  addresses the alteration of the flow rapidity profile. Here, the two parameters are treated as done in the corresponding paper [23].

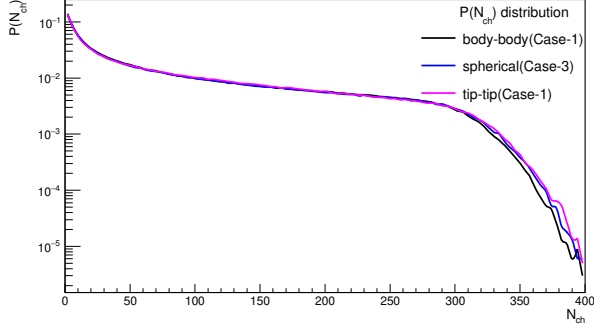
**Deformation:-** As we have mentioned previously, Ru has intrinsic quadrupole deformation and Zr has octupole [20]. But the default HYDJET++ model doesn't have a deformed nuclear density profile. So, the deformed nuclear density function was included. The Modified Woods Saxon distribution function in spherical polar coordinates can be expressed as:-

$$\rho(r, \theta, \psi) = \frac{\rho_0}{1 + \exp\left(\frac{r - R(1 + \beta_2 Y_{20} + \beta_4 Y_{40})}{a}\right)}$$

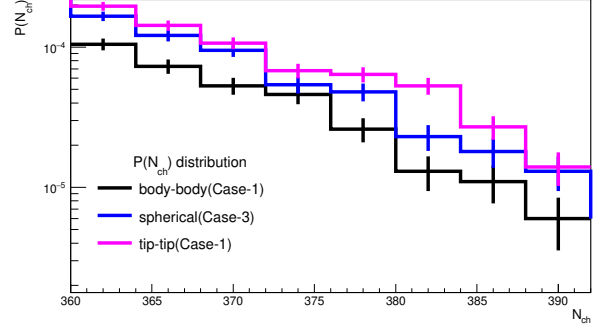
where,  $\rho_0 = \rho_0^{\text{const}} + \text{correction}$ ,  $\rho_0^{\text{const}} = \frac{\text{Mass}}{\text{Volume}} = \frac{3A}{4\pi R_A^3}$ ,  $R_A = R(1 + \beta_2 Y_{20} + \beta_4 Y_{40})$ ,  $R_l =$

Species	Case-1 [38]				Case-2 [39]				Case-3 [40]			
	$R$ (fm)	$a$ (fm)	$\beta_2$	$\beta_3$	$R$ (fm)	$a$ (fm)	$\beta_2$	$\beta_3$	$R$ (fm)	$a$ (fm)	$\beta_2$	$\beta_3$
$^{96}_{44}\text{Ru}$	5.085	0.46	0.158	0	5.063	0.485	0.154	0	5.067	0.500	0	0
$^{96}_{40}\text{Zr}$	5.020	0.46	0.080	0	4.960	0.536	0.062	0.202	4.965	0.556	0	0

TABLE I: Woods-Saxon parameters for  $^{96}_{44}\text{Ru}$  and  $^{96}_{40}\text{Zr}$  nuclei.



(a)



(b)

FIG. 1: Variation of total charged particle multiplicity ( $N_{ch}$ ) for body-body (case-1), spherical (case-3) and tip-tip (case-1) collisions.

$R_0(1 + \beta_2 Y_{20} + \beta_4 Y_{40})$ ,  $R = R_0 A^{1/3}$  and  $R_0 = 1.15 fm$ . The correction term is calculated as  $\rho_0(\pi f/R_A)^2$ , where  $Y_{20} = \sqrt{\frac{5}{16\pi}}(3 \cos^2 \theta - 1)$ , and  $Y_{40} = \frac{3}{16\sqrt{\pi}}(35 \cos^4 \theta - 30 \cos^2 \theta + 3)$  are the spherical harmonics.

The HYDJET++ model uses a cylindrical polar coordinate system. So we transformed this nuclear density profile function from spherical ( $r, \theta, \psi$ ) to cylindrical coordinates ( $\rho, \psi, z$ ). The relationships of  $\theta = \tan^{-1}(z/r)$  and  $\theta = \tan^{-1}(r/z)$  for body-body and tip-tip configurations, respectively, are used for the coordinate transformation. Here,  $r$  is used instead of  $\rho$  in the cylindrical polar coordinate system to avoid possible confusion with the nuclear density function ( $\rho$ ). By changing  $\psi$ , one can get many other configurations. However, in this study, we are limiting ourselves to body-body and tip-tip configurations only.

### III. RESULTS AND DISCUSSIONS

The extreme configurations, such as tip-tip and body-body in isobar collisions, provide insight into the influence of nuclear structure on the dynamics of heavy-ion collisions. These extreme configurations amplify certain signals and suppress some others. A higher octupole deformation causes a reflection asymmetry in the shape of Zr [20]. Given that the octupole deformation study in the low-energy zone is unreliable [41], we can employ high-energy collisions to probe nucleon configurations event-by-event and get insight into nuclear deformations.

The introduction of deformation parameters alters the nuclear density distribution, consequently modifying the effective nuclear radius. In the spherical case, the radius is given by a simple empirical formula  $R_0 = r_0 A^{1/3}$ , but in the deformed case, it is dependent on  $\theta$ . The spherical harmonics are used to describe the nuclear shape. The detailed mathematical formulation can be found in the corresponding papers [42, 43]. To enable a meaningful comparison with experimental results, we consider a spherical configuration (case-3 in Table-I) based on parameters from density functional theory calculations [40]. In addition, two deformed configurations are included: case-1 from [38] and case-2 from [39], as also summarized in Table-I.

In Fig. 1(a), the  $N_{ch}$  distribution of Ru for body-body, spherical, and tip-tip configurations is shown. For better resolution, we have shown the tail portion separately in Fig. 1(b). It is clearly visible that the tails of the charged hadron distributions do not coincide. It means that when the nuclear shape differs, or nuclei collide in different specific orientations, then the same centrality class corresponds to different impact parameters, and hence different numbers of participants ( $N_{part}$ ) are being produced. The  $N_{part}$  distribution of all those is displayed in Fig. 2. In HYDJET++, the impact parameter range is provided as an input to define the desired centrality class for the generated events. Since the multiplicity distribution varies for each configuration, we performed centrality selection for each configuration separately. The centralities were assigned based on the multiplicity of charged hadrons using the integral fraction method [30], and the impact parameters corresponding to the  $\langle N_{ch} \rangle$  values

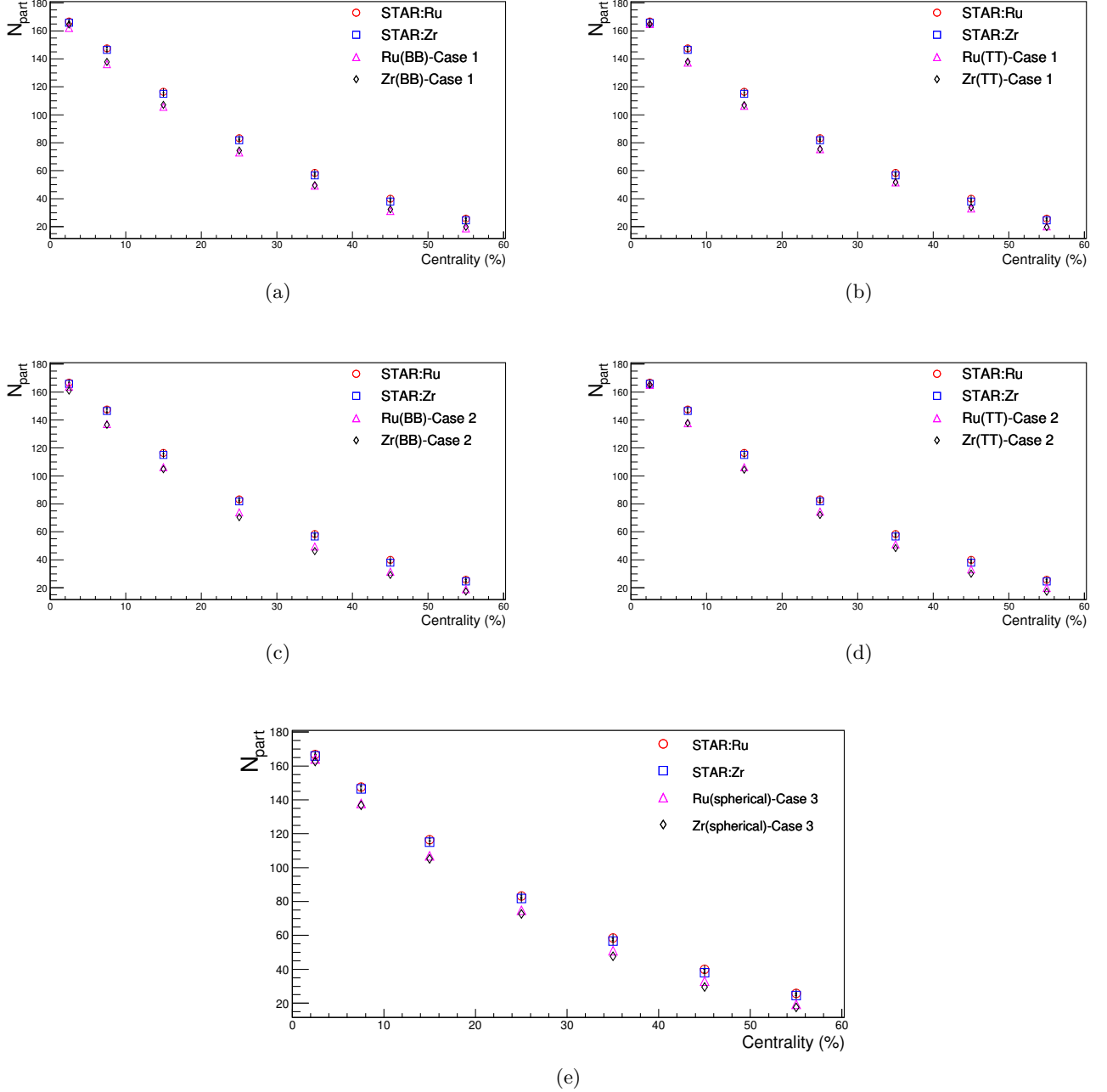


FIG. 2: Variation of  $N_{\text{part}}$  with respect to centrality for (a) body-body (case-1), (b) tip-tip (case-1), (c) body-body (case-2), (d) tip-tip (case-2), (e) spherical (case-3) collisions.

were used as inputs.

### A. Pseudorapidity distribution

The pseudorapidity distribution is the measure of the charged particle yield per unit pseudorapidity interval. It gives information about the fireball's evolution. A wider  $\eta$  distribution indicates a larger and strongly expanding fireball; meanwhile, a smaller distribution points to

a narrower and asymmetric fireball. The pseudorapidity distribution typically depends on the collision centrality and shape of the colliding nuclei.

In Fig. 3, we present the pseudorapidity distributions of charged hadrons produced in isobaric collisions of Ru+Ru and Zr+Zr for the most central (0–5%) and peripheral (50–60%) collisions. Ru has slight differences in the values of  $a$  and  $\beta_2$  between case-1 and case-2. In contrast, Zr exhibits larger variations in both  $a$  (from 0.46 to 0.536 fm) and  $\beta_2$  (from 5.02 to 4.96 fm) in the two cases,

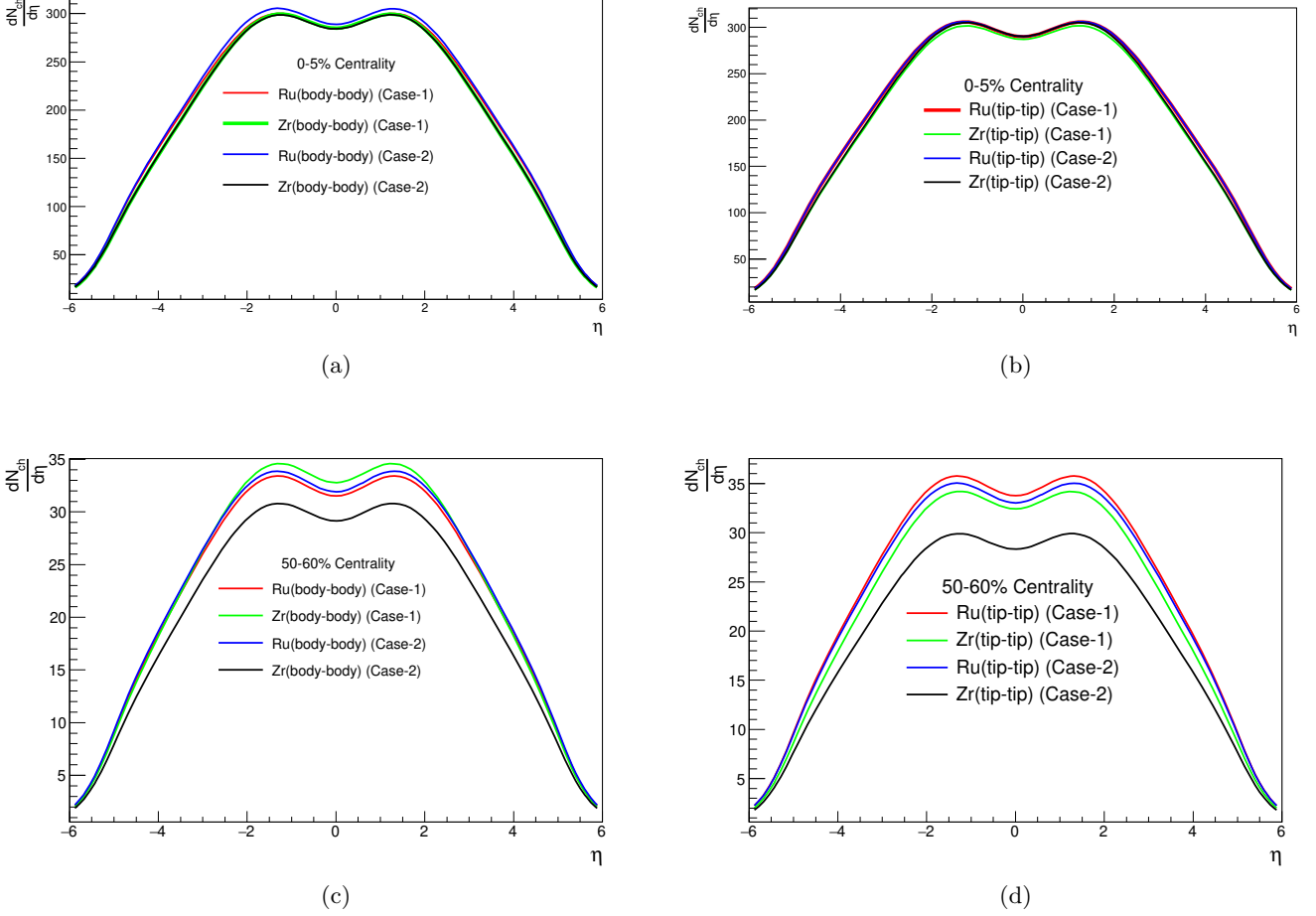


FIG. 3: Variation of  $\frac{dN_{ch}}{d\eta}$  with respect to  $\eta$  for (a) body-body (0-5% centrality), (b) tip-tip (0-5% centrality), (c) body-body (50-60% centrality), (d) tip-tip (50-60% centrality) collisions.

along with the inclusion of  $\beta_3 = 0.202$  in case-2. The deformation parameters ( $\beta$ ) directly influence the nuclear geometry, while  $a$  controls the thickness of the overlapping surface. A larger  $a$  makes the edge of the nucleus more diffuse, thereby modifying the overlap region during collisions. To improve visualization, the plots of Figs. 3(a) and 3(b) are enlarged and displayed separately in Fig. 4.

Figures 3(a) and 3(b) depict the pseudorapidity distribution  $\frac{dN_{ch}}{d\eta}$  as a function of  $\eta$  for the 0-5% centrality range. At  $\eta = 0$ , the central (0-5%) body-body collisions with the case-1 parameter set yield a higher charged-hadron multiplicity for Zr than for Ru. Since  $a$  is identical for both nuclei in this case, the main difference arises from  $\beta_2$ . Zr, having a smaller  $\beta_2$ , is closer to spherical, resulting in a larger central overlap zone and, therefore, a higher multiplicity. In contrast, Fig. 4(a) demonstrates that, within the same centrality range, body-body collisions of Ru with the case-2 parameters yield consistently higher  $N_{ch}$  across the entire pseudorapidity range. This behavior can be attributed to Ru's denser core, resulting

from its smaller value of  $a$ .

The  $\frac{dN_{ch}}{d\eta}$  distributions for tip-tip collisions in the most central class (0-5%) exhibit a noticeable overlap between Ru and Zr around  $\eta = 0$  in case-2. Ru has a comparatively larger quadrupole deformation parameter ( $\beta_2 = 0.154$ ) than that of Zr ( $\beta_2 = 0.062$ ). A larger value of  $\beta_2$  in tip-tip collisions results in a more elongated nuclear shape along the beam axis, which enhances the production of charged particles ( $N_{ch}$ ). A higher surface diffuseness ( $a$ ) also contribute to the increased effective overlap volume, particularly in the central collision zone (Zr:  $a = 0.536$  and Ru:  $a = 0.485$ ). While Ru benefits from a higher value of  $\beta_2$ , Zr compensates for it with a larger value of  $a$  and asymmetry in shape ( $\beta_3$ ) that is present in Zr. Thus, this overlap in  $\frac{dN_{ch}}{d\eta}$  curve shows a hint of the positive effect of  $\beta_3$  in the charged hadron production of Zr. In contrast, while considering case-1, Ru's more prominent elliptic form causes it to produce more particles than Zr in central (0-5%) tip-tip collisions [Fig. 4(c)] over the whole pseudorapidity range.

In peripheral collisions (50-60% centrality) for the

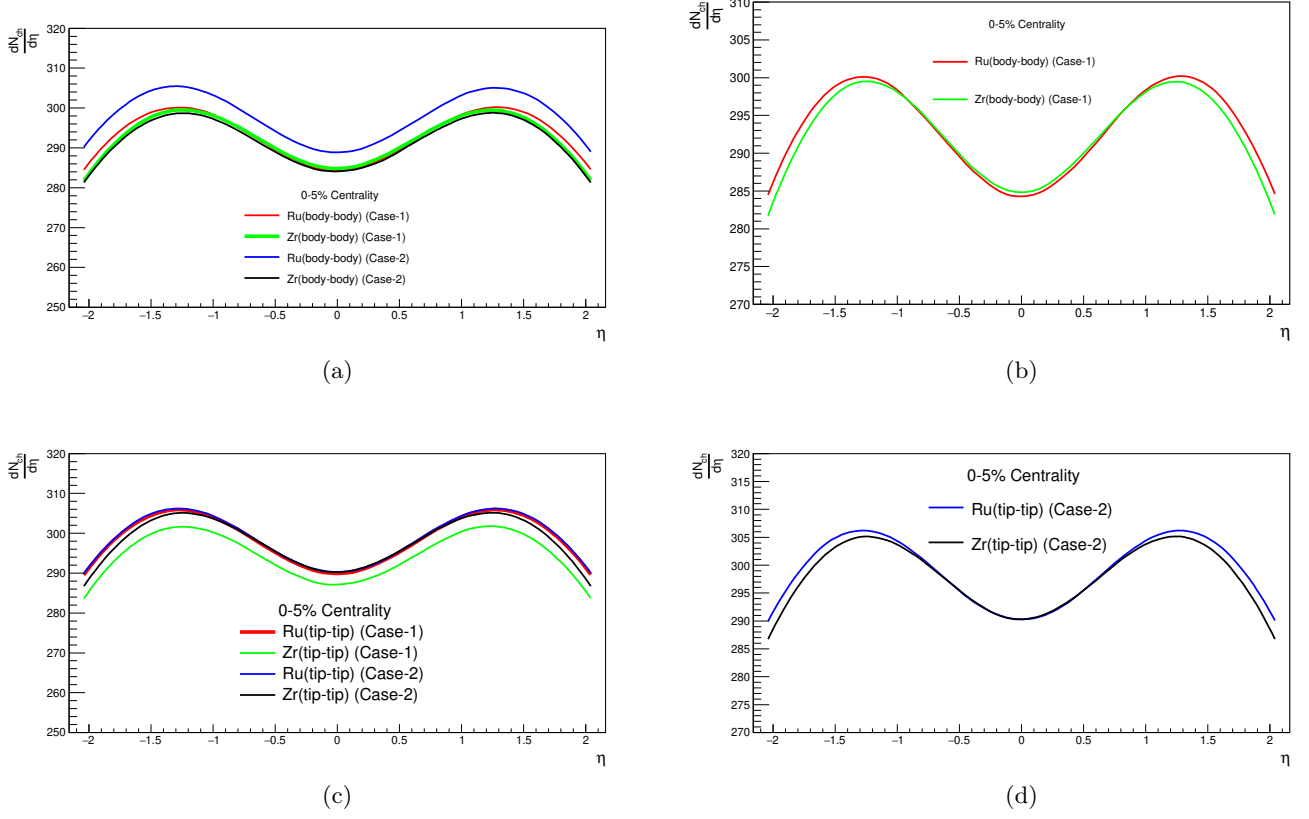


FIG. 4: A magnified view of Fig. 3(a) is shown in (a) and (b) here. Again, an enlarged view of Fig. 3(b) is presented in (c) and (d).

body-body case [Fig. 3(c)], Ru exhibits a higher  $N_{\text{ch}}$  value around  $\eta = 0$  when case-2 parameter sets are used for both nuclei. Since Zr has more surface diffuseness ( $a$ ) and less elongation ( $\beta_2$ ), Zr should have a higher value of  $N_{\text{ch}}$ . A possible contributing factor is the asymmetry from  $\beta_3$  in case-2, which may reduce the symmetry of the overlap by introducing surface bulges. This in turn decreases the charged hadron production in peripheral body-body collisions of Zr. This trend reverses for both nuclei when they collide in the case-1 configuration. In body-body collisions of case-1, Zr has a higher value of  $N_{\text{ch}}$  around  $\eta = 0$ . The reason is that in case-1, the surface diffuseness parameter  $a$  is maintained constant for both Ru and Zr, thereby removing its impact. Under these conditions, the role of nuclear shape becomes dominant. Ru has a much larger quadrupole deformation ( $\beta_2 = 0.158$ ) compared to Zr ( $\beta_2 = 0.08$ ). However, in peripheral body-body collisions, the greater elongation of Ru reduces the transverse overlap. The Zr, with its more compact shape and the same surface diffuseness, provides a larger effective overlap area, resulting in a higher charged-particle multiplicity.

Now, analyzing Fig. 3(d), Ru has a slightly more  $N_{\text{ch}}$  value than Zr in case-1. Here, Zr doesn't have the advantage of a higher value of  $a$ . Therefore, it confirms that,

without higher surface diffuseness, Zr underpredicts in peripheral tip-tip collisions. This suggests that the effects of  $\beta_2$  dominate in peripheral tip-tip collisions for the case-1 configuration. Hence, even in peripheral tip-tip collisions, Ru has better tip-tip overlap with case-1 parameters. Now in the same figure, the Zr (tip-tip, case-2) curve (black) is the lowest among all four curves in this 50-60% centrality bin. This is strange, as Zr has a larger value of  $a$ , which would be expected to increase the overlap zone, particularly in peripheral tip-tip collisions. So this dip in the black curve is likely due to the negative effect of the term  $\beta_3$  in Zr. Overall, for peripheral tip-tip collisions in case-2, the surface diffuseness ( $a$ ) enhances the overlap, whereas the asymmetry introduced by  $\beta_3$  reduces  $N_{\text{ch}}$ .

The effect of Woods-Saxon parameters in extreme configurations can be further verified by comparison with the spherical case. In Fig. 5, we have shown the ratio of charged-hadron multiplicity in body-body and tip-tip collisions relative to that in the spherical case, for multiple configurations and two centrality classes. The key observations are summarized below.

In Fig. 5(a), within the 0-5% centrality range, case-2 lies above unity while case-1 remains below. For Ru, which has only  $\beta_2$ , one would expect case-1, with its

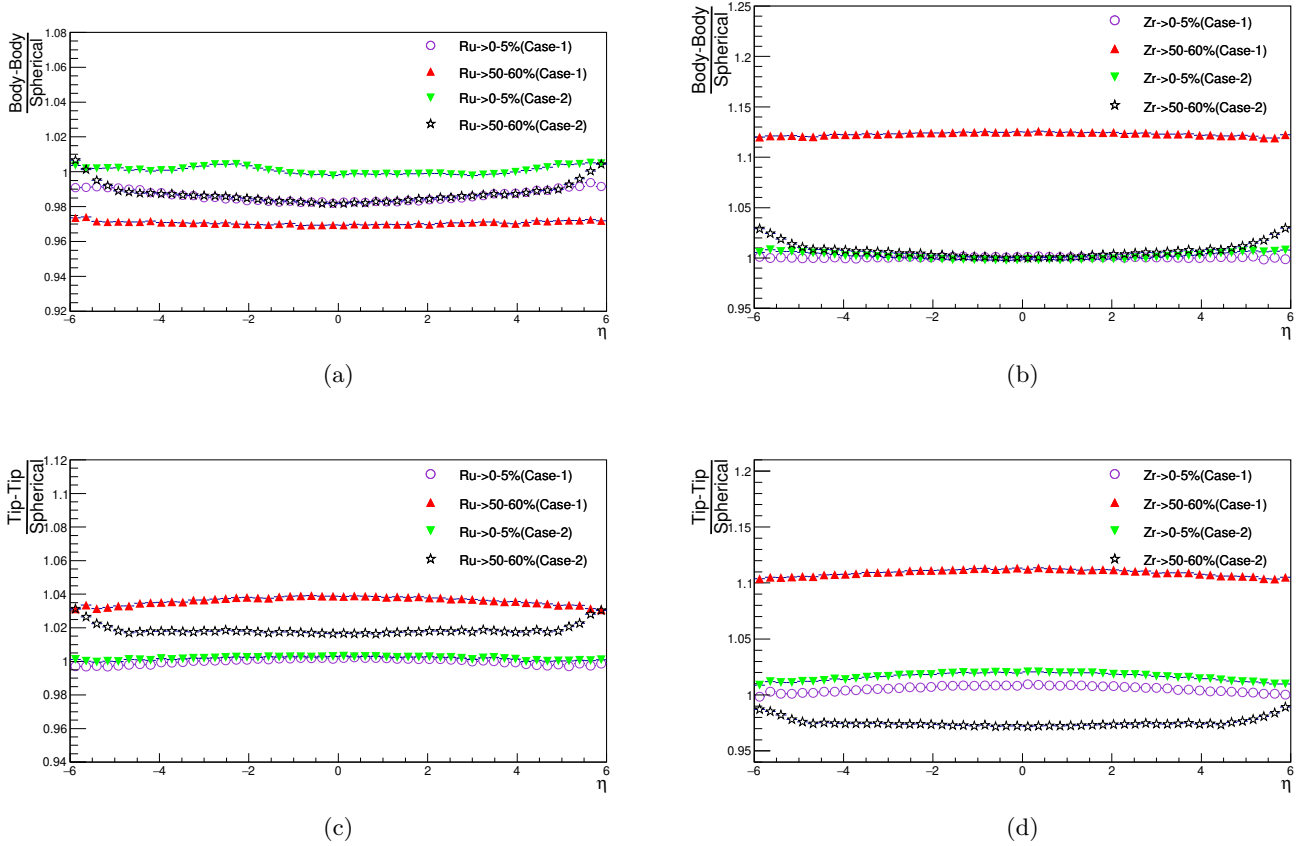


FIG. 5: Ratio of pseudorapidity distributions for deformed to spherical configurations: (a) body-body to spherical for Ru, (b) body-body to spherical for Zr, (c) tip-tip to spherical for Ru, and (d) tip-tip to spherical for Zr.

higher  $\beta_2$  value, to lie above case-2 in the body-body collisions. However, the results show the opposite behavior. This is due to the higher surface diffuseness ( $0.46 \rightarrow 0.485$  fm) in case-2, which led to a higher overlap area and hence higher  $N_{ch}$ . Therefore, in central body-body collisions,  $a$  has a dominant effect than  $\beta_2$ . In the same figure, in 50-60% centrality, case-2 again has more multiplicity of charged hadrons than case-1, due to the higher surface diffuseness. In peripheral collisions, only the outer skin of the nucleus overlaps, where diffuseness directly affects the particle density. A higher value of  $a$  makes the surface more extended and smoother, allowing slightly more nucleons to participate even at larger impact parameters.

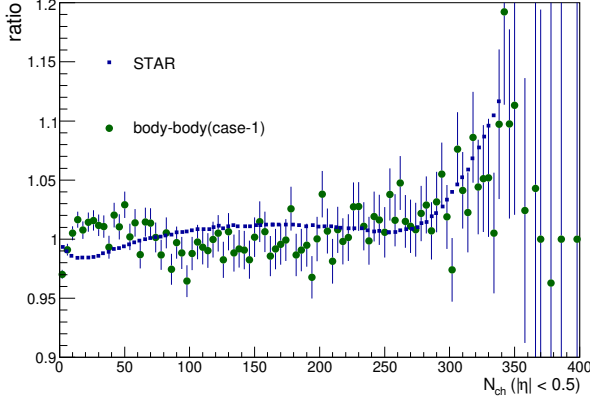
Fig. 5(c) presents the tip-tip to spherical ratio of Ru. For 0-5% centrality, the curves are nearly aligned, with case-2 showing a slightly higher ratio than case-1. Since case-2 has less elongation, its blunter tip contributes to the higher observed  $N_{ch}$ . Additionally, the higher surface diffuseness of case-2 further enhances  $N_{ch}$  in central collisions. In contrast, for the peripheral case (50-60%), case-1 (red triangles) exhibits a higher ratio than case-2 (black stars). In case-1, the sharper nuclear surface (smaller  $a$ ) creates a denser overlap zone. This produces slightly more participant nucleons and a higher  $N_{ch}$ , de-

spite the larger surface diffuseness in Case-2.

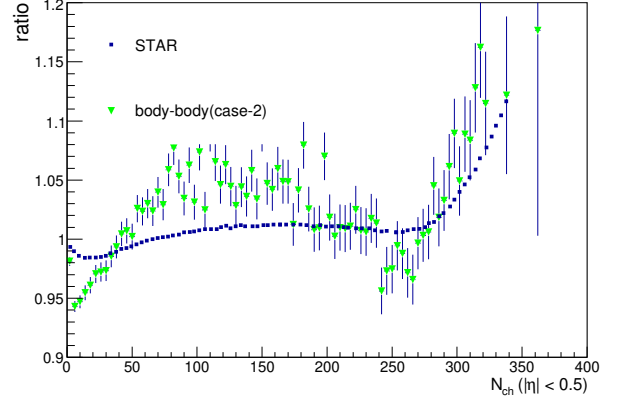
In Fig. 5(b), a Zr+Zr body-body collision is shown. Even with different  $\beta_2$  deformations and different  $a$  values, central collision (0-5%) ratios are nearly identical. The presence of  $\beta_3$  has no discernible effect in Zr's central body-body collisions. The ratios are close to unity, so it means that the overlapping region is not much affected by deformation. Particle production for the body-body configuration (red triangles) increases considerably in the peripheral collisions due to the decreased quadrupole deformation. By the same reasoning, the ratio in case-2 (black stars) would also be expected to increase. This indicates that the asymmetry introduced by  $\beta_3$  reduces the multiplicity in case-2.

In the remaining panel Fig. 5(d), case-1 and case-2 are also closely positioned in the 0-5% centrality range. However, a subtle distinction can be observed here in contrast to the near overlap of body-body to spherical ratio for Zr in Fig. 5(b). The value of the surface diffuseness of case-2 is greater than case-1. In Fig. 5(d), for central tip-tip (0-5%) collisions, surface diffuseness exhibits a more positive and dominant effect. Again, for peripheral collisions (50-60%), case-1 ratio is much larger than the case-2 ratio. Since the  $\beta_2$  values are very close

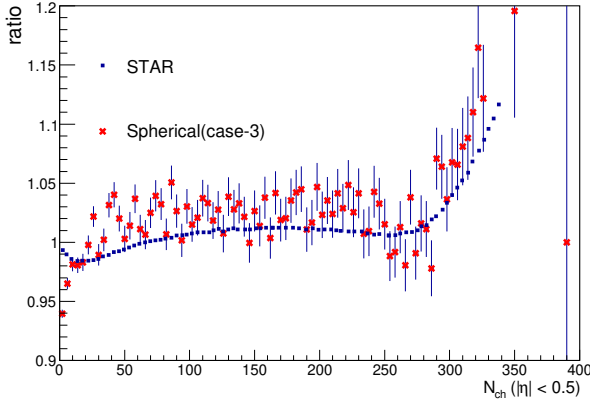




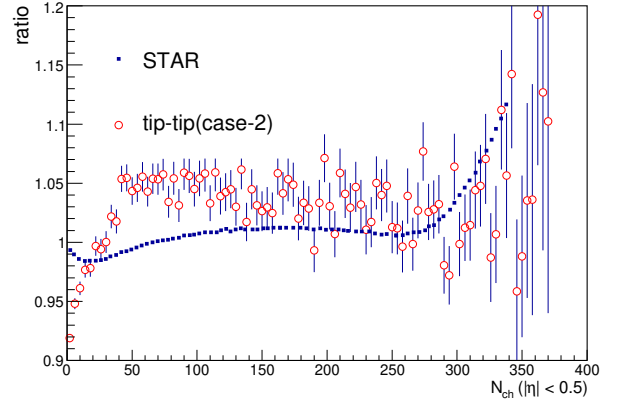
(a)



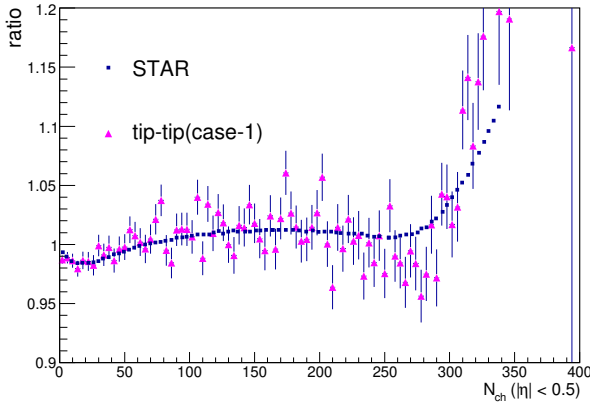
(a)



(b)



(b)



(c)

FIG. 6:  $\frac{P(N_{\text{ch}})^{\text{Ru}}}{P(N_{\text{ch}})^{\text{Zr}}}$  distributions for (a) body-body (case-1), (b) spherical (case-3), and (c) tip-tip (case-1) configurations.

FIG. 7:  $\frac{P(N_{\text{ch}})^{\text{Ru}}}{P(N_{\text{ch}})^{\text{Zr}}}$  distributions for (a) body-body (case-2) and (b) tip-tip (case-2).

( $\beta_2 = 0.08 \rightarrow 0.062$ ) and the diffuseness  $a$  is higher for case-2, a dip is not expected in case-2. The observed dip in peripheral tip-tip collisions (Zr+Zr) [black stars in Fig. 5(d)] shows that  $\beta_3$  has a negative effect on the charged hadron production in peripheral tip-tip collisions.

## B. $N_{\text{ch}}$ distribution analysis

We have examined the centrality-dependent behavior of the  $P(N_{\text{ch}})$  ratio between Ru and Zr for various collision configurations.  $P(N_{\text{ch}})$  is the probability distribution of charged hadron multiplicity.

In Fig. 6(b), the case-3 WS density parametrization is selected based on the recent calculations of energy density functional theory (DFT) [40], assuming the nuclei as spherical. The ratio  $\frac{P(N_{\text{ch}})^{\text{Ru}}}{P(N_{\text{ch}})^{\text{Zr}}}$  rises at large multiplicities due to the extended high- $N_{\text{ch}}$  tail in Ru+Ru collisions. This stems from the smaller root-mean-square size



of Ru compared to Zr in DFT calculations, which leads to higher energy density and an increased number of binary nucleon-nucleon collisions in central events [44]. In mid-central to semi-peripheral regions ( $N_{\text{ch}} = 50 - 300$ ), the ratios are consistent with the experimental trend. The dip in the ratio at peripheral collisions (between  $N_{\text{ch}} = 0 - 50$ ) can be attributed to a thicker skin of Zr, which leads to a more diffuse distribution of peripheral density.

A similar high- $N_{\text{ch}}$  trend, initially observed in the spherical configuration for 0–5% centrality, is also present in central tip-tip (case-1) [Fig. 6(c)] and body-body (case-2) [Fig. 7(a)] collisions. For peripheral (50–60%) body-body collisions in case-2 [Fig. 7(a)], the ratio is well below unity, consistent with the earlier spherical-case explanation that a thicker nuclear surface yields a more diffuse peripheral density distribution. Meanwhile, for the tip-tip of case-1 [Fig. 6(c)], since the surface diffuseness is the same for both Ru and Zr, so the dip is not found in the peripheral collision zone. By analogous reasoning, the body-body collisions of case-1 [Fig. 6(a)] does not display any dip in the ratio at the peripheral (50–60%) collisions.

The body-body collisions of case-1 [Fig. 6(a)] and the tip-tip collisions of case-2 [Fig. 7(b)] do not exhibit the characteristic peak in higher multiplicity (0–5%). We discuss each case individually below. In case-1, surface diffuseness is the same for Ru and Zr. So when they collide in a body-body orientation in a central collision, Zr shows increased charged hadron production due to its larger shape. But in the tip-tip collisions of case-2, the scenario is different. Here, Ru has a smaller surface diffuseness. Hence, in central tip-tip collisions, Zr+Zr exhibits higher charged-hadron production due to its more diffused tips. In mid-central to peripheral region ( $N_{\text{ch}}=50-300$ ), the body-body collisions of case-1 [Fig. 6(a)] is below the experimental plot, while tip-tip (case-2) [Fig. 7(b)] is above it. This is most likely because, in body-body collisions, the Zr+Zr system forms a dense collision zone due to its less elliptic shape. While in the tip-tip case (case-2), due to the added asymmetry in Zr ( $\beta_3$ ) the  $\frac{P(N_{\text{ch}})^{\text{Ru}}}{P(N_{\text{ch}})^{\text{Zr}}}$  ratio stays above unity.

The effect of Zr's asymmetry is most evident in body-body collisions (case-2) [Fig. 7(a)], where both the most central and peripheral events can be explained by the same reasoning previously provided for spherical nuclei. Although the simulated body-body curve for case-1 [Fig. 6(a)] lies below unity in the mid-centrality range, the corresponding case-2 curve [Fig. 7(a)] exceeds unity in the same range. This indicates that the  $\beta_3$  parameter in Zr reduces the production of charged hadrons in body-body collisions.

### C. $v_2$ ratio

In Fig. 8, we have shown the centrality-wise  $v_2$  ratio distribution for different WS parameters and different

configurations. All the curves (with different conditions) are compared with the STAR data of  $v_2\{\text{EP}\}$  [17].

In the body-body collision of case-1, the small quadrupole deformation in Zr exaggerated the  $\langle v_2 \rangle$  ratio (the blue squares). The ratio always stays above unity. While in the tip-tip collisions of case-1 (the green triangles), the ratio goes below unity. In tip-tip collisions, the nuclei overlap along the longer axis. A more elliptic nuclear shape gives a greater deformation along the major axis. When a collision happens between such elliptically deformed nuclei for a tip-tip configuration, it results in a more spherical fireball. So in case-1, the larger  $\beta_2$  has reduced the anisotropy. This explains why the  $v_2$  ratio consistently remains below one in all centralities in the tip-tip collisions of case-1.

Next, we include the octupole deformation using case-2 of the parameter set. The tip-tip configuration without  $\beta_3$  shows no substantial deviation from the corresponding distribution with  $\beta_3$  (green triangles vs. pink rhombus). This shows that the octupole deformation parameter does not have a significant effect on the elliptic flow in tip-tip collisions. However, the body-body curve for case-2 (red triangles) lies significantly below, falling even beneath the spherical case. This means the octupole deformation enhances  $\langle v_2 \rangle$  in Zr+Zr collisions for the body-body configuration. Even in the spherical case, the ratio is less than one. Since both nuclei are completely round in this case, intrinsic nuclear deformation does not contribute to  $\langle v_2 \rangle$ . Thus, it can be concluded that surface diffuseness and centrality have a significant impact on the elliptic flow ratio in collisions of spherical nuclei.

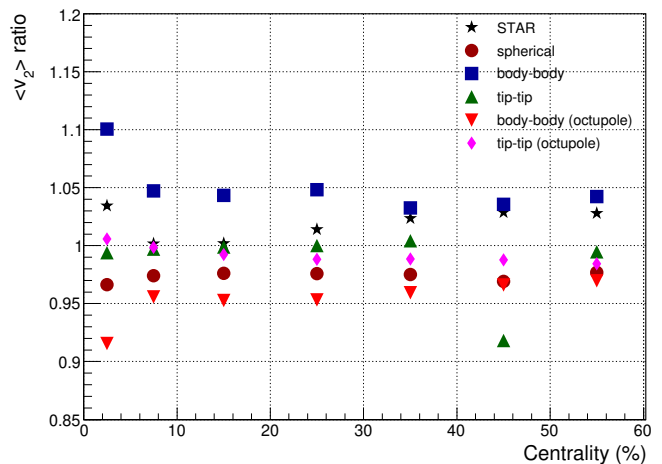


FIG. 8: Centrality-wise  $v_2$  distribution for different configurations.

### IV. SUMMARY

The primary focus of most isobar collision studies concentrates on CME signatures like  $\gamma$  correlator. However,

nuclear deformation parameters, which significantly influence the flow-related background to CME signals, have not been thoroughly investigated. High-energy relativistic heavy-ion collisions offer a promising way to probe the deformation-driven phenomena more precisely. We found that the quadrupole deformation ( $\beta_2$ ) and the surface diffuseness parameter ( $a$ ) significantly affect the elliptic flow ( $v_2$ ) and particle multiplicity. We have demonstrated that  $\beta_3$  has a positive impact on the charged hadron production in the most-central (0 – 5%) tip-tip collisions through analysis of the  $\eta$  distributions. Meanwhile, in peripheral tip-tip collisions (50 – 60%), the effect of  $\beta_3$  is negative. The ratio of  $\eta$  distributions of deformed to spherical nuclei were also studied. In 50–60% centrality,  $\beta_3$  has a negative effect on particle production for the body-body collisions. The effect of  $\beta_3$  can also be seen on the  $N_{\text{ch}}$  distribution with respect to centrality. The reduced charged hadron production in Zr suggests that  $\beta_3$  negatively affects charged hadron production in mid-central ( $N_{\text{ch}} = 50\text{--}300$ ) body-body collisions. In centrality-wise  $v_2$  distribution plots, the introduction of octupole deformation enhances the elliptic flow in Zr+Zr collisions. The effect of  $\beta_3$  is more prominent in body-body collisions. Based on our find-

ings, we suggest that the extreme collision geometries can be a useful tool to understand background CME-signals in heavy-ion collisions. In future studies, such techniques may prove instrumental in disentangling the complex background contributions, thereby facilitating a more accurate exploration of the chiral magnetic effect (CME).

## DATA AVAILABILITY

Data will be made available upon request.

## ACKNOWLEDGEMENTS

BKS sincerely acknowledges financial support from the Institute of Eminence (IoE), BHU Grant number 6031. AD acknowledges the financial support through the Institute fellowship from IIITDM Jabalpur. SRN acknowledges the financial support from the UGC Non-NET fellowship and IoE research incentive during the research work.

- 
- [1] Y. Nir, [arXiv:hep-ph/9911321 [hep-ph]].
  - [2] R. Fleischer, Eur. Phys. J. ST **233** (2024) no.2, 391-408 doi:10.1140/epjs/s11734-024-01127-0 [arXiv:2402.00710 [hep-ph]].
  - [3] R. Aaij *et al.* [LHCb], Phys. Rev. Lett. **134** (2025) no.10, 101801 doi:10.1103/PhysRevLett.134.101801 [arXiv:2411.12178 [hep-ex]].
  - [4] J. C. Collins and M. J. Perry, Phys. Rev. Lett. **34** (1975), 1353 doi:10.1103/PhysRevLett.34.1353
  - [5] E. V. Shuryak, Phys. Lett. B **78** (1978), 150 doi:10.1016/0370-2693(78)90370-2
  - [6] D. Kharzeev, R. D. Pisarski and M. H. G. Tytgat, Phys. Rev. Lett. **81** (1998), 512-515 doi:10.1103/PhysRevLett.81.512 [arXiv:hep-ph/9804221 [hep-ph]].
  - [7] D. Kharzeev and R. D. Pisarski, Phys. Rev. D **61** (2000), 111901 doi:10.1103/PhysRevD.61.111901 [arXiv:hep-ph/9906401 [hep-ph]].
  - [8] P. D. Morley and I. A. Schmidt, Z. Phys. C **26** (1985), 627 doi:10.1007/BF01551807
  - [9] D. E. Kharzeev and J. Liao, Nucl. Phys. News **29** (2019) no.1, 26-31 doi:10.1080/10619127.2018.1495479
  - [10] V. Skokov, A. Y. Illarionov and V. Toneev, Int. J. Mod. Phys. A **24** (2009), 5925-5932 doi:10.1142/S0217751X09047570 [arXiv:0907.1396 [nucl-th]].
  - [11] Y. Feng, S. A. Voloshin and F. Wang, [arXiv:2502.09742 [nucl-ex]].
  - [12] K. Fukushima, D. E. Kharzeev and H. J. Warringa, Phys. Rev. D **78** (2008), 074033 doi:10.1103/PhysRevD.78.074033 [arXiv:0808.3382 [hep-ph]].
  - [13] D. Kharzeev, Phys. Lett. B **633** (2006), 260-264 doi:10.1016/j.physletb.2005.11.075 [arXiv:hep-ph/0406125 [hep-ph]].
  - [14] D. E. Kharzeev, L. D. McLerran and H. J. Warringa, Nucl. Phys. A **803** (2008), 227-253 doi:10.1016/j.nuclphysa.2008.02.298 [arXiv:0711.0950 [hep-ph]].
  - [15] M. I. Abdulhamid *et al.* [STAR], Phys. Rev. Res. **6** (2024) no.3, L032005 doi:10.1103/PhysRevResearch.6.L032005 [arXiv:2308.16846 [nucl-ex]].
  - [16] Y. Feng, Y. Lin, J. Zhao and F. Wang, Phys. Lett. B **820** (2021), 136549 doi:10.1016/j.physletb.2021.136549 [arXiv:2103.10378 [nucl-ex]].
  - [17] M. Abdallah *et al.* [STAR], Phys. Rev. C **105** (2022) no.1, 014901 doi:10.1103/PhysRevC.105.014901 [arXiv:2109.00131 [nucl-ex]].
  - [18] X. L. Zhao and G. L. Ma, Phys. Rev. C **106** (2022) no.3, 034909 doi:10.1103/PhysRevC.106.034909 [arXiv:2203.15214 [nucl-th]].
  - [19] F. Li, Y. G. Ma, S. Zhang, G. L. Ma, Q. Shou and Q. Y. Shou, Phys. Rev. C **106** (2022) no.1, 014906 doi:10.1103/PhysRevC.106.014906 [arXiv:2201.10994 [nucl-th]].
  - [20] C. Zhang and J. Jia, Phys. Rev. Lett. **128** (2022) no.2, 022301 doi:10.1103/PhysRevLett.128.022301 [arXiv:2109.01631 [nucl-th]].
  - [21] P. F. Kolb and U. W. Heinz, [arXiv:nucl-th/0305084 [nucl-th]].
  - [22] S. Acharya *et al.* [ALICE], Phys. Lett. B **834** (2022), 137393 doi:10.1016/j.physletb.2022.137393 [arXiv:2111.06106 [nucl-ex]].
  - [23] S. Pandey and B. K. Singh, J. Phys. G **49** (2022) no.9, 095001 doi:10.1088/1361-6471/ac81e1 [arXiv:2107.01880]

- [hep-ph]].
- [24] J. D. Bjorken, Phys. Rev. D **27** (1983), 140-151 doi:10.1103/PhysRevD.27.140
  - [25] P. Steinberg, Acta Phys. Hung. A **24** (2005), 51-57 doi:10.1556/APH.24.2005.1-4.8 [arXiv:nucl-ex/0405022 [nucl-ex]].
  - [26] I. P. Lokhtin, L. V. Malinina, S. V. Petrushanko, A. M. Snigirev, I. Arsene and K. Tywoniuk, Comput. Phys. Commun. **180** (2009), 779-799 doi:10.1016/j.cpc.2008.11.015 [arXiv:0809.2708 [hep-ph]].
  - [27] L. V. Bravina, I. P. Lokhtin, L. V. Malinina, S. V. Petrushanko, A. M. Snigirev and E. E. Zabrodin, Eur. Phys. J. A **53** (2017) no.11, 219 doi:10.1140/epja/i2017-12420-5 [arXiv:1709.08602 [hep-ph]].
  - [28] I. P. Lokhtin and A. M. Snigirev, Eur. Phys. J. C **45** (2006), 211-217 doi:10.1140/epjc/s2005-02426-3 [arXiv:hep-ph/0506189 [hep-ph]].
  - [29] T. Sjostrand, S. Mrenna and P. Z. Skands, JHEP **05** (2006), 026 doi:10.1088/1126-6708/2006/05/026 [arXiv:hep-ph/0603175 [hep-ph]].
  - [30] M. L. Miller, K. Reygers, S. J. Sanders and P. Steinberg, Ann. Rev. Nucl. Part. Sci. **57** (2007), 205-243 doi:10.1146/annurev.nucl.57.090506.123020 [arXiv:nucl-ex/0701025 [nucl-ex]].
  - [31] R. Baier, Y. L. Dokshitzer, A. H. Mueller and D. Schiff, Phys. Rev. C **64** (2001), 057902 doi:10.1103/PhysRevC.64.057902 [arXiv:hep-ph/0105062 [hep-ph]].
  - [32] B. Andersson, Camb. Monogr. Part. Phys. Nucl. Phys. Cosmol. **7** (1997), 1-471 Cambridge University Press, 1998, ISBN 978-1-009-40129-6, 978-1-009-40125-8, 978-1-009-40128-9, 978-0-521-01734-3, 978-0-521-42094-5, 978-0-511-88149-7 doi:10.1017/9781009401296
  - [33] N. S. Amelin, R. Lednicky, T. A. Pocheptsov, I. P. Lokhtin, L. V. Malinina, A. M. Snigirev, I. A. Karpenko and Y. M. Sinyukov, Phys. Rev. C **74** (2006), 064901 doi:10.1103/PhysRevC.74.064901 [arXiv:nucl-th/0608057 [nucl-th]].
  - [34] N. S. Amelin, R. Lednicky, I. P. Lokhtin, L. V. Malinina, A. M. Snigirev, I. A. Karpenko, Y. M. Sinyukov, I. Arsene and L. Bravina, Phys. Rev. C **77** (2008), 014903 doi:10.1103/PhysRevC.77.014903 [arXiv:0711.0835 [hep-ph]].
  - [35] H. Sorge, Phys. Rev. Lett. **78** (1997), 2309-2312 doi:10.1103/PhysRevLett.78.2309 [arXiv:nucl-th/9610026 [nucl-th]].
  - [36] Z. W. Lin, C. M. Ko, B. A. Li, B. Zhang and S. Pal, Phys. Rev. C **72** (2005), 064901 doi:10.1103/PhysRevC.72.064901 [arXiv:nucl-th/0411110 [nucl-th]].
  - [37] B. Schenke, S. Jeon and C. Gale, Phys. Rev. C **82** (2010), 014903 doi:10.1103/PhysRevC.82.014903 [arXiv:1004.1408 [hep-ph]].
  - [38] W. T. Deng, X. G. Huang, G. L. Ma and G. Wang, Phys. Rev. C **94** (2016), 041901 doi:10.1103/PhysRevC.94.041901 [arXiv:1607.04697 [nucl-th]].
  - [39] W. van der Schee, Y. J. Lee, G. Nijs and Y. Chen, Phys. Lett. B **856** (2024), 138953 doi:10.1016/j.physletb.2024.138953 [arXiv:2307.11836 [nucl-th]].
  - [40] H. j. Xu, H. Li, X. Wang, C. Shen and F. Wang, Phys. Lett. B **819** (2021), 136453 doi:10.1016/j.physletb.2021.136453 [arXiv:2103.05595 [nucl-th]].
  - [41] J. Jia, G. Giacalone, B. Bally, J. D. Brandenburg, U. Heinz, S. Huang, D. Lee, Y. J. Lee, C. Loizides and W. Li, *et al.* Nucl. Sci. Tech. **35** (2024) no.12, 220 doi:10.1007/s41365-024-01589-w [arXiv:2209.11042 [nucl-ex]].
  - [42] W. Horiuchi and T. Inakura, PTEP **2021** (2021) no.10, 103D02 doi:10.1093/ptep/ptab087 [arXiv:2106.13454 [nucl-th]].
  - [43] S. Geldhof, M. Kortelainen, O. Beliuskina, P. Campbell, L. Caceres, L. Cañete, B. Cheal, K. Chrysalidis, C. S. Devlin, R. P. de Groote, A. de Roubin, T. Eronen, Z. Ge, W. Gins, A. Koszorus, S. Kujanpää, D. Nesterenko, A. Ortiz-Cortes, I. Pohjalainen, I. D. Moore, A. Raggio, M. Reponen, J. Romero, and F. Sommer, Phys. Rev. Lett. **128**, 152501 (2022), doi:10.1103/PhysRevLett.128.152501
  - [44] H. Li, H. j. Xu, J. Zhao, Z. W. Lin, H. Zhang, X. Wang, C. Shen and F. Wang, Phys. Rev. C **98** (2018) no.5, 054907 doi:10.1103/PhysRevC.98.054907 [arXiv:1808.06711 [nucl-th]].